SUPPORTING INFORMATION

Synthesis of graphene nanoribbons with defined mixed edge-site sequence by surface assisted polymerization of (1,6)-dibromopyrene on Ag(110)

Marco Smerieri[1], Igor Píš[2,3,*], Lara Ferrighi[4], Silvia Nappini[3], Angelique Lusuan[1,5], Cristiana Di Valentin,[4] Luca Vaghi,[4] Antonio Papagni,[4] Mattia Cattelan[6,§], Stefano Agnoli[6], Elena Magnano[3,7], Federica Bondino[3] and Letizia Savio[1*]

[1]*IMEM-CNR, UOS Genova, Via Dodecaneso 33, 16146 Genova, IT*

[2]*Elettra-Sincrotrone Trieste S.C.p.A., S.S. 14 km 163.5, 34149 Basovizza (TS), IT*

[3]*IOM-CNR, Laboratorio TASC, S.S. 14 km 163.5, 34149 Basovizza (TS), IT*

[4]*Dipartimento di Scienza dei Materiali, Università di Milano-Bicocca, Via R. Cozzi 55, 20125 Milano, IT*

[5] *Dipartimento di Fisica, Università di Genova, Via Dodecaneso 33, 16146 Genova, IT*

[6]*Department of Chemical Science, University of Padova. Via F. Marzolo 1, 35131 Padova, IT*

[7]*Department of Physics, University of Johannesburg, PO Box 524, Auckland Park, 2006, Johannesburg, South Africa*

*Corresponding authors: letizia.savio@imem.cnr.it, igor.pis@elettra.eu

§ Present address: School of Chemistry, University of Bristol, Bristol BS8 1TS, United Kingdom

1. Temperature-Programmed X-ray Photoelectron Spectroscopy (TP-XPS)

High-resolution and temperature programmed synchrotron-excited XPS measurements were carried out at the BACH beamline at Elettra synchrotron (Trieste, Italy), in an UHV chamber with the base pressure below 1×10^{-9} mbar and equipped with a hemispherical electron energy analyzer (VG Scienta model R3000). The sample normal, the X-ray beam and photoelectron emission direction were all in the same horizontal plane. The photoemission

spectra were recorded at the emission angle of 60° from the surface normal with linearly polarized X-rays in normal incidence geometry. Both Br 3d and C 1s core levels were excited with a photon energy hν=379 eV. A total energy resolution of 0.15 eV was calculated from the width of the Fermi edge. All photoemission binding energies are referenced to the substrate Fermi level. The substrate temperature during the annealing experiment was monitored by a thermocouple attached to the edge of the Ag(110) crystal. The heating rate during the temperature programmed XPS (TP-XPS) measurements was 15 °C/min. Both C 1s and Br 3d spectra were recorded during the temperature ramp from RT to 450°C with 5 °C temperature difference between two successive carbon or bromine spectra. The work function was determined by measuring the variation of the low-energy secondary electrons cut-off edge. The hemispherical electron spectrometer and the following experimental conditions were employed: hν=47.10 eV, normal emission geometry, sample bias voltage of -9.13 V. Temperature dependent WF measurements were recorded in the same manner as the TP-XPS of the core-levels using the same nominal DBP coverage of 1.2 ML. The WF changes are referred to the value after the deposition, which was measured to be 4.64 eV.

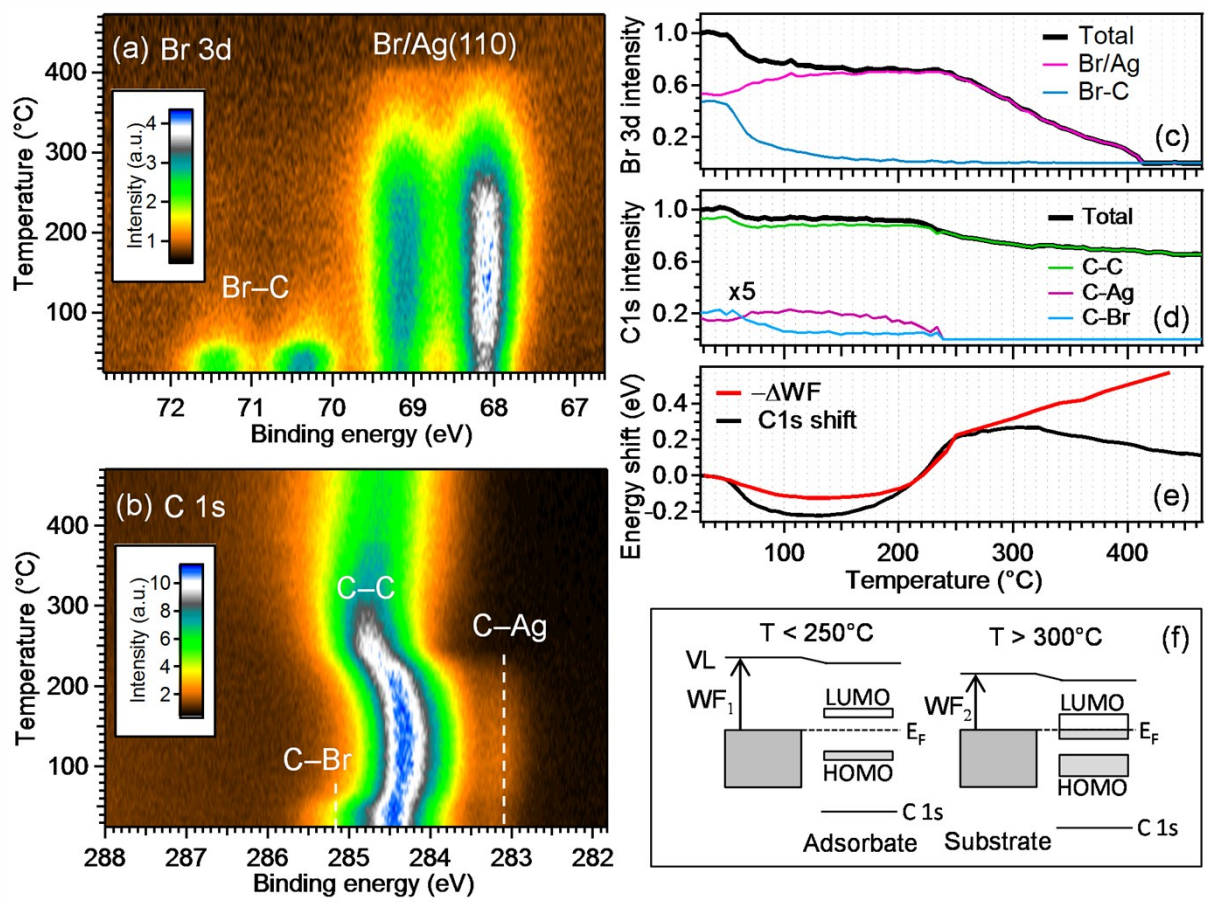

Figure S1. (a) Br 3d and (b) C 1s temperature dependent spectra shown as two-dimensional intensity plots. (c) Temperature dependence of the intensity of the total Br 3d signal and of the two main components. (d) Same as (c) for the total C 1s intensity and for the three main C 1s spectral features. (e) Binding energy shift of the C 1s spectrum component from the aromatic carbon atoms (labeled as C-C component) as a function of annealing temperature, plotted together with the sample work function (WF) variation with respect to the values measured at RT. (f) Schematic energy band diagrams illustrating vacuum level (left) and Fermi level (right) pinning scenarios.

The intensity plots in Figures S1a and S1b show the evolution of C 1s and Br 3d spectra at increasing temperature. The plots in Figures S1c and S1d display the temperature dependence of the total spectral intensities and the intensities of the main spectral components. A small intensity loss of both Br 3d and C 1s signals is observed between RT and 80°C. It is assigned to desorption of the second layer DBP molecules, which are not interacting with the substrate. The residual intensity, which is stable up to about 220 °C, corresponds to full monolayer coverage. From 50 to 100 °C intense Br–C dissociation is well visible in both carbon and bromine spectra (decrease of Br–C components). Simultaneously, Br atoms spill over the silver substrate (increase of Br/Ag component in Br 3d spectrum) and the carbon radicals bind with the substrate adatoms (increase of C–Ag component in C 1s spectrum). The chemical transformations revealed by XPS and the formation of long molecular chains observed by the STM microscopy imply the organometallic nature of the chains, with Br atoms adsorbed on the silver substrate in between the 1D protopolymers. These protopolymers prevail on the surface up to the temperature of 220 °C. The vanishing C–Ag component in the C 1s spectrum between 220 °C and 240 °C indicates decomposition of the organometallic species and beginning of the transition to a new structure. STM microscopy revealed formation of C–C covalent polymers with much different surface orientation in comparison with the organometallic protopolymers. To achieve such rearrangement, surface migration and rotation of the DBP biradicals must occur in the transition temperature range. The energy barrier of the thermally induced covalent polymerization of DBP on Ag(110) must be close to the desorption energy of the molecular precursor, as suggested by the small drop of the C 1s intensity in this transition temperature range (240–300 °C, Figure 3d). From the temperature of 250 °C, also the intensity of the Br signal starts to decrease until it vanishes completely at T> 400 °C. TPR spectroscopy has revealed that most of the chemisorbed bromine desorbs from the surface in the form of HBr. The source of hydrogen atoms are the debrominated DBP molecules, which must undergo at least partial dehydrogenation in order to form the C–C intermolecular bonds. At T>410 °C, the bromine is not present anymore on the surface and the C 1s overall intensity, as well as its spectral shape, is quite stable. Small but systematic shift towards lower E_b is attributed to continuous dehydrogenation and interconnection between the conjugated polymers, as observed by STM.

The E_b variation of the C 1s component corresponding to the aromatic carbon atoms of the pyrene group (Figure S1e) can reflect the energy alignment at the adsorbate-metal interface[1]. To understand the nature of the C 1s core-level shift, the sample work function (WF) was measured during the temperature ramp and the change of WF is plotted together with the C 1s binding energy shift in Figure S1e. The match between the core-level shift and WF changes at the temperatures below 260 °C points to the vacuum-level alignment scenario[2, 3] schematically depicted in Figure S1f, on the left. In this scenario, typical for weakly interacting adsorbate/substrate systems, changes in the vacuum level rigidly shift all molecular levels by the same amount. The observed WF change is mostly dominated by the amount of chemisorbed Br atoms. The WF is increasing with the Br spill over the substrate in agreement with expectations[4]. However, the WF starts rapidly to decrease above 200 °C. This sudden change must be related with chemical and conformational changes or structural distortions of the molecules since the amount of chemisorbed Br is stable at this temperature. The continuing WF drop with temperature finally results in a Fermi level pinning[5], which is verified by the E_b(C 1s)

independence on work function variation. Although the C 1s shift towards higher binding energies upon annealing is sometimes assigned to intermolecular C–C coupling in literature,[6, 7] here we demonstrate it can be solely the effect of the energy level alignment at the molecule–metal interface.

2. Near-Edge X-ray Absorption Fine Structure Spectroscopy (NEXAFS)

To further explore the electronic structure and geometry of the DBP adsorbate layer, polarization dependent C K-edge NEXAFS spectroscopy was carried out. The NEXAFS spectroscopy was performed at the BACH beamline at Elettra synchrotron (Trieste, Italy) in Auger electron yield mode recording C KVV Auger electrons with the hemispherical electron analyzer fixed at a kinetic energy of 260 eV. The C K-edge NEXAFS spectra were normalized to the signal from the clean Ag(110) substrate recorded under identical conditions. Polarization-dependent measurements were performed with the linearly polarized x-ray beam impinging on the surface at normal incidence (θ=90°) and at grazing incidence (θ=20°), respectively.

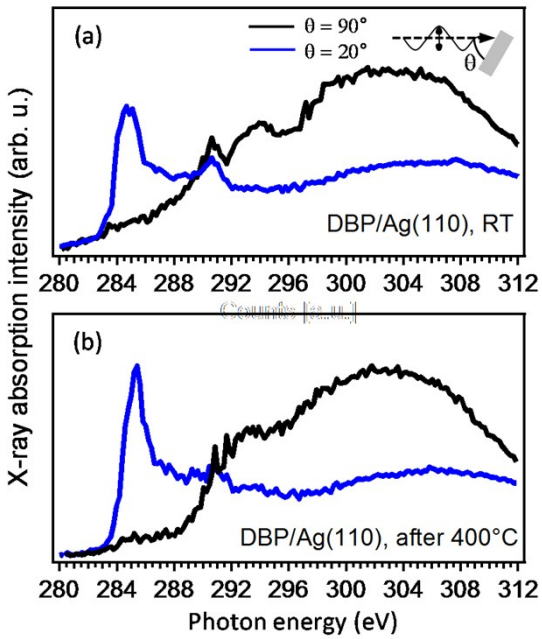

Figure S2. Polarization-dependent C K-edge NEXAFS of a DBP thin layer deposited on Ag(110) at RT (a) and after the annealing to 400 °C (b).

NEXAFS spectra probe the partially-filled or unoccupied states and carbon bonds to its intra and extra-molecular neighbors. Moreover, orientation of the molecules with respect to the substrate can be readily determined exploiting linearly polarized synchrotron radiation. The excitation from the occupied C 1s core-level to unoccupied π^* orbital in a planar π–conjugated carbon system reaches the maximum intensity when the electric field vector of the linearly polarized synchrotron radiation is vertical to the molecular plane (parallel to $2p_z$ orbitals). On the contrary, the transition into σ^* molecular orbitals reaches the maximum for the polarization vector parallel to the molecular plane.

The C K-edge NEXAFS spectra of DBP deposited on Ag(110), obtained at two different polarization geometries, are reported in Figure S2a. The energy region up to 290 eV is

dominated by π^* resonances. The strong resonance around 284.7 eV corresponds to the transition from C 1s occupied core-level to the lowest unoccupied molecular levels (LUMOs)[8,9]. The broader shape of the main π^* resonance with respect to pure pyrene indicates multicomponent character, which can be assigned to non-equivalent carbon atoms with bonds to Br substituent and Ag substrate. The energy region 288–290 eV has presumably a mixed character assigned to $\sigma_{C-H}^*$and π_2^* resonances[10,11]. The energy region above 292 eV contains σ^* resonances. The significant reduction of the π^* resonance intensity and enhanced intensity of σ^* resonances for the x-ray polarization vector parallel to the surface plane is a clear evidence of nearly flat adsorption geometry. The flat-lying geometry is further enhanced after the annealing at 400 °C, as evident from Figure S2b. The low energy π^* resonance narrowed after the annealing, in accord with the Br desorption and transformation of the organometallic intermediates into the covalent polymers. The spectrum in Figure S2b shows also reduced intensity in the region with σ_{C-H}^* resonances, in agreement with the dehydrogenation observed by TPR. The overall NEXAFS spectrum shape resembles the typical lineshape of graphene nanostructures, such as graphene nanoribbons.[6, 12]

3. Statistical data on STM images.

The average width of the GNRs declared in the paper (9.9±0.6 Å) was determined from statistical analysis over a wide number of nanostructures. Details are reported in table T1.

Preparation	Direction off <1-10>	# of GNRs	Width
Θ<1ML 2 min. @ 150 °C 1 min. @ 400 °C		1302	(10.0±1.0) Å
Θ>1ML 2 min. @ 150 °C 1 min. @ 400 °C		77	(10.1±1.2) Å
Θ>1ML 15 min. @ 150 °C 3 min. @ 400 °C	-55°	201	(10.0±0.6) Å
	-30°	165	(9.8±0.6) Å
	average	366	(9.9±0.6) Å

Table T1. Summary of the statistical analysis performed to determine the GNRs width. Series with different directions have been separated only for the highly odered preparation.

4. Bias dependence of STM images.

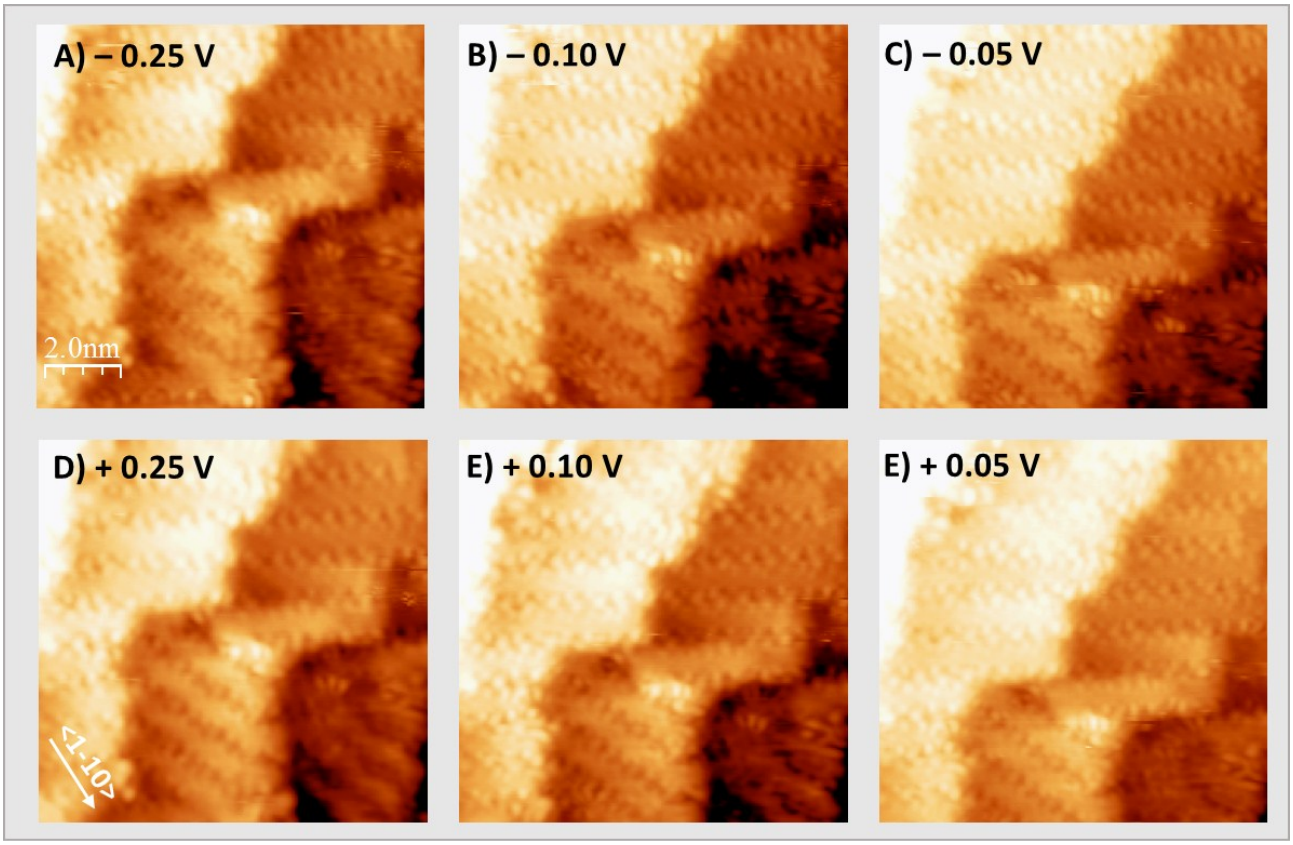

Figure S3. Series of high resolution STM images recorded parametric in bias voltage. No evident bias dependence can be detected in the investigated V range, in agreement with the simulated result of Figure S9. Image size 10x10 nm^2.

5. Density Functional Theory simulations

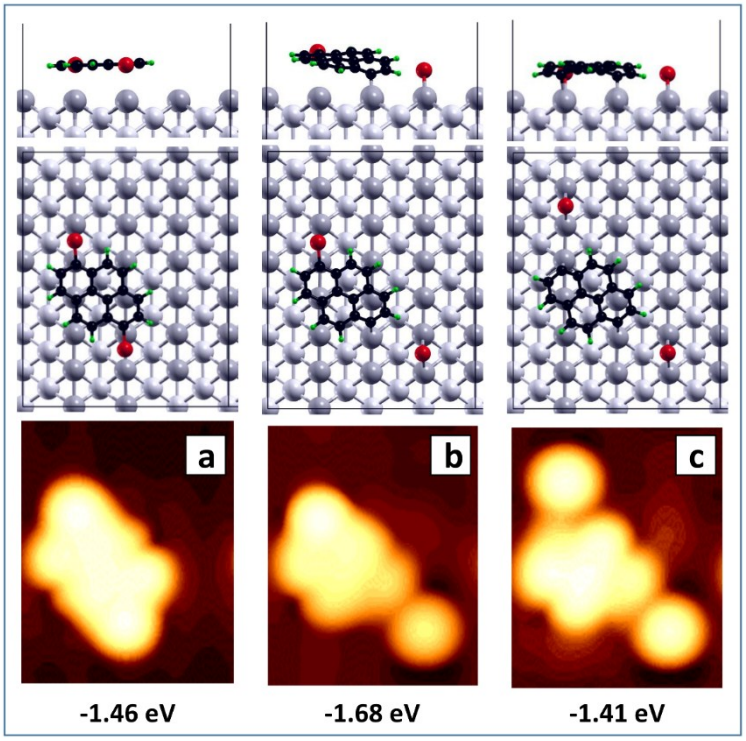

Figure S4 Side and top views of the optimized strucure (top row) and STM simulated images (bottom row) for a DBP monomer adsorbed on Ag(110). a) Physisorbed DBP, b) first debromination and c) second debromination. The intact DBP unit appears with a very homogeneous contrast. After the full debromination, the radical skeleton appears with four lobes corresponding to the benzene rings, whereas the Br atoms adsorbed on the Ag substrate appear as sharp and round bright spots.

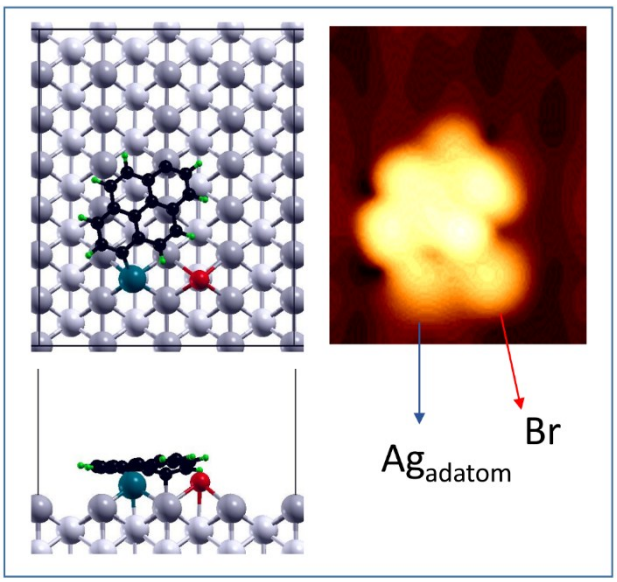

Figure S5 Left: Top and side views of a fully debrominated DBP monomer with a radical carbon bonded directly to the Ag substrate and the other to a silver adatom. In the proximity, a Br atom is also deposited. Right: The

corresponding simulated STM image shows clearly the four lobes of the DBP skeleton, while the Ag and Br atoms look like roundish bright spots.

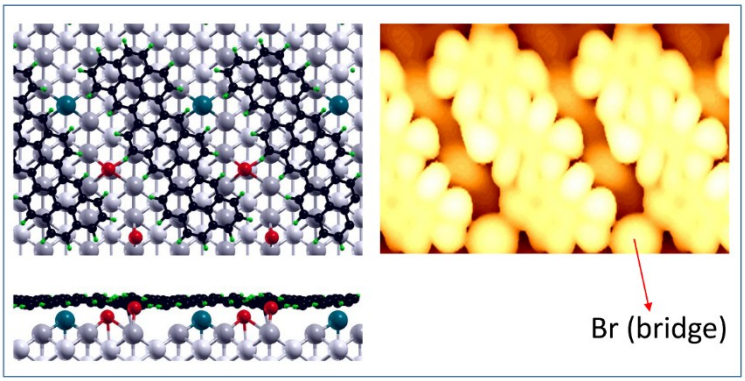

Figure S6 Left: Top and side view of the conjugated DBP trimer, together with one Ag adatom (blue) and two Br atoms adsorbed either in hollow or bridge position. Right: simulated STM images showing that the Br atom in bridge postion has a brighter contrast with respect to the Br atom in hollow position.

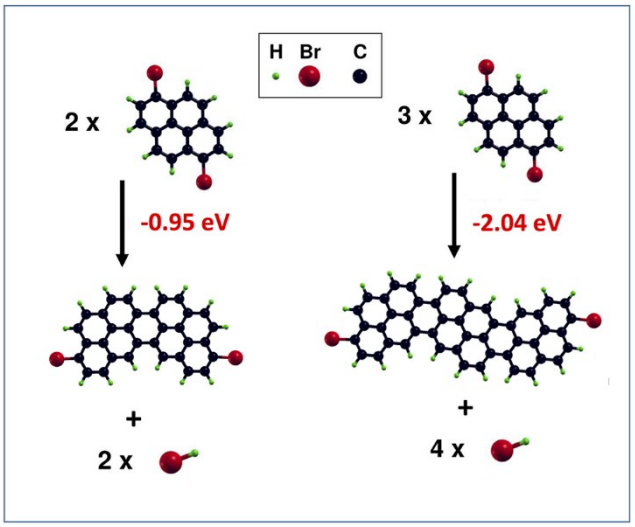

Figure S7 Formation of graphene nanoribbons in gas-phase, with the relase of HBr molecules. The energy gain associated with the formation of two C-C bonds between DBP units is about 1 eV.

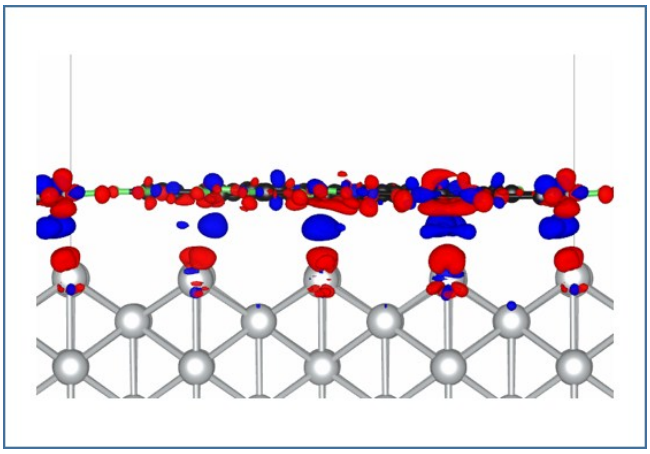

Figure S8 Electron density map[13] difference for the adsorbed ribbon on Ag(110). Red colour: loss of electron density; Blue color: gain of electron density.

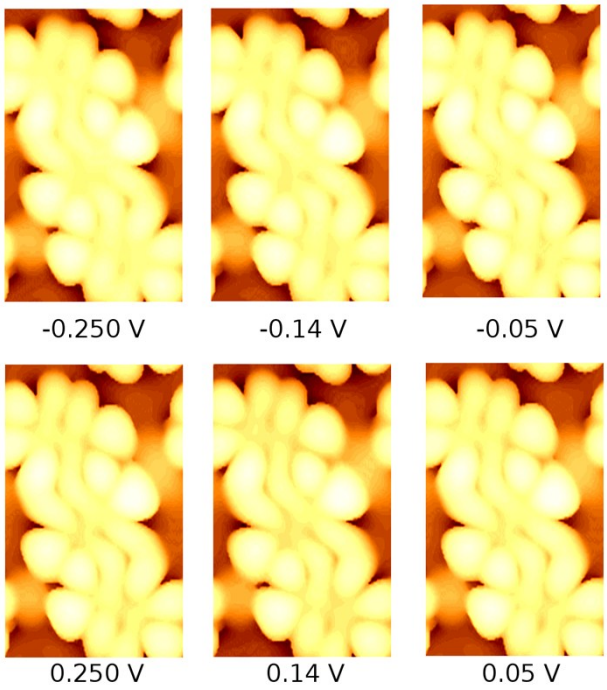

Figure S9 Simulated STM images of the graphene nanoribbons using different bias voltages. The images show a negligible bias dependence in agreement with the experimental findings.

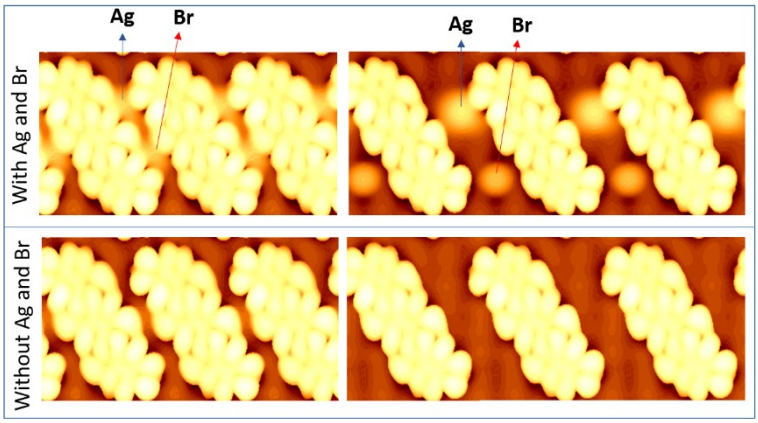

Figure S10. Simulated STM images of graphene nanoribbons formed by homochiral DBP radicals at different coverage (in a 3×7 or in a 4×7 supercell). Top: Ribbons in presence on Ag and Br atoms. Bottom: Ribbons without additional Ag and Br adatoms.

References

1. A. El-Sayed, P. Borghetti, E. Goiri, C. Rogero, L. Floreano, G. Lovat, D. Mowbray, J. Cabellos, Y. Wakayama and A. Rubio, *ACS nano*, 2013, **7**, 6914-6920.
2. S. Winkler, J. Frisch, R. Schlesinger, M. Oehzelt, R. Rieger, J. Räder, J. P. Rabe, K. Müllen and N. Koch, *The Journal of Physical Chemistry C*, 2013, **117**, 22285-22289.
3. A. Kahn, N. Koch and W. Gao, *Journal of Polymer Science Part B: Polymer Physics*, 2003, **41**, 2529-2548.
4. H. G. Zimmer, A. Goldmann, R. Courths and H. Saalfeld, *Surface science*, 1986, **173**, 465-478.
5. N. Koch, *Journal of Physics: Condensed Matter*, 2008, **20**, 184008.
6. A. Batra, D. Cvetko, G. Kladnik, O. Adak, C. Cardoso, A. Ferretti, D. Prezzi, E. Molinari, A. Morgante and L. Venkataraman, *Chemical Science*, 2014, **5**, 4419-4423.
7. D. M. Giovannantonio, E. M. Garah, J. Lipton-Duffin, V. Meunier, L. Cardenas, Y. F. Revurat, A. Cossaro, A. Verdini, D. F. Perepichka, F. Rosei and G. Contini, *ACS Nano*, 2013, **7**, 8190– 8198
8. H. Ågren, O. Vahtras and V. Carravetta, *Chemical Physics*, 1995, **196**, 47-58.
9. R. Kakavandi, S.-A. Savu, A. Caneschi, T. Chassé and M. Casu, *Chemical Communications*, 2013, **49**, 10103-10105.
10. G. Sanďı, K. Song, K. A. Carrado and R. E. Winans, *Carbon*, 1998, **36**, 1755–1758.
11. J. A. Horsley, J. Stöhr, A. P. Hitchcock, D. C. Newbury and A. L. Johnson, *The Journal of Chemical Physics*, 1985, **83**, 6099.
12. K. A. Simonov, N. A. Vinogradov, A. S. Vinogradov, A. V. Generalov, E. M. Zagrebina, N. Mårtensson, A. A. Cafolla, T. Carpy, J. P. Cunniffe and A. B. Preobrajenski, *The Journal of Physical Chemistry C*, 2014, **118**, 12532-12540.
13. K. Momma and F. Izumi, *Journal of Applied Crystallography*, 2011, **44**, 1272-1276.